

# A bio-inspired method for direct measurement of local wall shear rates with micrometer localization using the multimeric protein von Willebrand factor as sensor molecule

Klaus Bonazza, Bernhard Scheichl, Johannes Frank, Hanspeter Rottensteiner, Gerald Schrenk, Gernot Friedbacher, Peter L. Turecek, Friedrich Scheiflinger, and Günter Allmaier

Citation: *Biomechanics* **11**, 044117 (2017); doi: 10.1063/1.5000503

View online: <http://dx.doi.org/10.1063/1.5000503>

View Table of Contents: <http://aip.scitation.org/toc/bmf/11/4>

Published by the [American Institute of Physics](#)

---

---

Looking for a specific instrument?

Easy access to the latest equipment.  
Shop the *Physics Today* Buyer's Guide.

PHYSICS TODAY

lasers imaging  
VACUUM EQUIPMENT instrumentation  
software MATERIALS  
cryogenics + MORE...

## A bio-inspired method for direct measurement of local wall shear rates with micrometer localization using the multimeric protein von Willebrand factor as sensor molecule

Klaus Bonazza,<sup>1,a)</sup> Bernhard Scheichl,<sup>2,3</sup> Johannes Frank,<sup>4</sup>  
Hanspeter Rottensteiner,<sup>5</sup> Gerald Schrenk,<sup>5</sup> Gernot Friedbacher,<sup>1</sup>  
Peter L. Turecek,<sup>5</sup> Friedrich Scheiflinger,<sup>5</sup> and Günter Allmaier<sup>1,b)</sup>

<sup>1</sup>*Institute of Chemical Technologies and Analytics, Vienna University of Technology, Getreidemarkt 9, A-1060 Vienna, Austria*

<sup>2</sup>*Institute of Fluid Mechanics and Heat Transfer, Vienna University of Technology, Getreidemarkt 9, A-1060 Vienna, Austria*

<sup>3</sup>*AC<sup>2</sup>T Research GmbH (Austrian Center of Competence for Tribology), Viktor-Kaplan-Straße 2/C, A-2700 Wiener Neustadt, Austria*

<sup>4</sup>*Joint Workshop of the Faculty of Technical Chemistry, Getreidemarkt 9, A-1060 Vienna, Austria*

<sup>5</sup>*Shire, Industriestraße 67, A-1221 Vienna, Austria*

(Received 3 January 2017; accepted 16 August 2017; published online 30 August 2017)

Wall shear rates are critical for a broad variety of fluidic phenomena and are taken into account in nearly every experimental or simulation study. Generally, shear rates are not observable directly but rather derived from other parameters such as pressure and flow, often assuming somehow idealized systems. However, there is a biological system which is able to constantly measure the wall shear as a part of a regulatory circuit: The blood circulation system takes advantage of shear rate sensor (protein)molecules (multimeric forms of von Willebrand Factor, VWF), which are dissolved in the blood plasma and dramatically change their conformation under shear conditions. The conformational changes are accompanied by several functional variations and therefore interplay with the regulation of the coagulation system. In this study, we use a recombinantly produced and therefore well-defined multimeric form of VWF as a sensor which directly responds to shear rates. Shear rates, up to  $32.000\text{ s}^{-1}$ , were obtained using a kind of micro-plate-to-plate rheometer capable of adsorbing shear-stretched VWF oligomeric molecules on a surface to conserve their differently stretched conformation and so allow detection of their elongation by atomic force microscopy. The laminar flow in this geometrically simple device has been characterized by adopting classical fluid dynamical models, in order to ensure well-known, stable shear rates which could be correlated quantitatively with an observed stretching of sensor molecules. *Published by AIP Publishing.* [<http://dx.doi.org/10.1063/1.5000503>]

### I. INTRODUCTION

Boundary conditions at solid/fluid-interfaces are critical for various fields and applications such as mass transport,<sup>1</sup> energy transport,<sup>1,2</sup> surface cleaning in food hygiene and medicine,<sup>3,4</sup> aerodynamics,<sup>1</sup> hydrodynamics, and blood coagulation.<sup>5,6</sup> The wall shear rate is an often inaccessible parameter. Much effort has been made in the past to measure local wall shear rates or shear stress. The first approaches were inspired from aerospace engineering and based on static

<sup>a)</sup>Present address: Harvard Medical School and Boston Children's Hospital, 3 Blackfan Circle, Boston, MA 02215, USA.

<sup>b)</sup>Author to whom correspondence should be addressed: [gunter.allmaier@tuwien.ac.at](mailto:gunter.allmaier@tuwien.ac.at).

hole pairs with separations in the mm or cm range.<sup>1,7</sup> A more recent work that uses porous elements can be seen as an improvement and miniaturization of these ideas.<sup>8</sup> Shear stress has also been determined by detection of the stress transferred to the solid, either by using deformable gels<sup>9</sup> or the optical stress response of liquid crystals.<sup>10</sup> Tracer particles have been used successfully to gain information about the local shear conditions in combination with sophisticated optical detection strategies,<sup>11</sup> and finally, diffusion controlled electrochemical reactions on the surface of small platinum electrodes were revealed to be shear rate dependent.<sup>12</sup> From all these methods, the two latter ones have probably the largest potential for downscaling given the latest progresses in high resolution optical microscopy (Nobel Prize for Chemistry 2014<sup>13</sup>) and the fact that microelectronics has reached the nanoscale.<sup>14</sup> The rise of microfluidics requires more and more direct detection and quantification of local wall shear rates with spatial resolution preferably in the micrometer or even sub-micrometer range. Due to the limitations in measuring such data, most studies rely on calculated wall shear rates.<sup>15</sup> Computational fluid dynamics (CFD) simulations depend on such new experimental data<sup>3,16</sup> especially when applied to micro- or nanofluidic systems.

Here, a bio-inspired approach for local shear rate detection is presented. Blood platelets in the circulation have the unique tendency to adhere on the surface of blood vessels and form stable plugs most efficiently in high shear conditions. The blood plasma contains shear rate sensor molecules (von Willebrand Factor, VWF) which are long multimeric (= oligomeric) (2 up to 40 covalently linked monomeric units) glycoprotein chains. At low shear rates, they circulate as loosely coiled globular structures with a diameter of  $\sim 90$  nm<sup>17</sup> as shown in the cartoon in Fig. 1 (left). At increasing shear rates, VWF gets uncoiled (Fig. 1, center), forms fibrils (Fig. 1, right), and becomes able to bind both blood platelets and injured vessel walls acting as a linker and binding the platelets to the injured tissue.

In this study, it is demonstrated that VWF can be used for detection of local shear rates also in an artificial system. Instead of detecting functional changes in the molecule,<sup>18</sup> like nature does, here the morphological transition is directly detected by atomic force microscopy (AFM). Shear rates were generated in a home-built device, which can be understood as an upgrade and a miniaturization of a high precision plate-to-plate rheometer (Fig. 2). These experiments can be seen as a progress to understand the stretching of VWF, which is essential for the physiological function of blood coagulation.<sup>19–21</sup> This system represents also a new strategy for local shear rate sensing in micro- and nanofluidics, which is the focus of the present work.

## II. EXPERIMENTAL

An aqueous buffer solution (Tris-buffered saline, TBS, consisting of 50 mM Tris, 150 mM NaCl, and  $0.4 \mu\text{M}$   $\text{MgCl}_2$ ) was fed to the device described below, thereby applying defined shear rates to the liquid. The buffer solution contained the chain-like shear force sensor molecules (von Willebrand Factor, VWF) at a low concentration ( $0.11 \mu\text{g/ml}$ ), which could be stretched at high shear conditions. The immobilization of these molecules on an appropriate surface (freshly cleaved mica) allowed a subsequent AFM imaging, which was used to determine the effect of shear rates on the sensor molecules. This experiment was performed at 5 different shear rates (Table I). Three independent mica samples were analyzed for every shear rate.

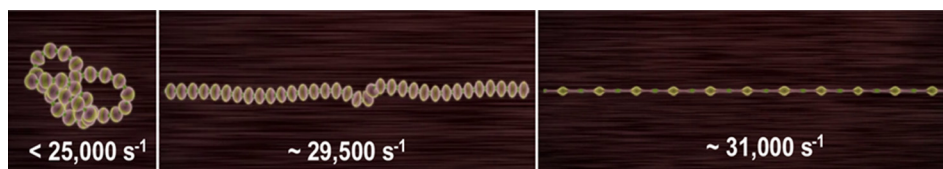


FIG. 1. Cartoon of the sensor molecule (von Willebrand Factor multimer) in solution at different shear rates based on AFM data. The chain-like molecule consists of periodically repeating mayor (yellow) and minor (green) globes and flexible (pink) interconnects. At low shear rates, it is loosely coiled ( $< 25\,000 \text{ s}^{-1}$ ), between  $\sim 25\,000 \text{ s}^{-1}$  and  $\sim 30\,000 \text{ s}^{-1}$ , there is a stochastic unravelling, and at  $\sim 31\,000 \text{ s}^{-1}$ , chains get strongly elongated and the diameter of globes start to decrease strongly.

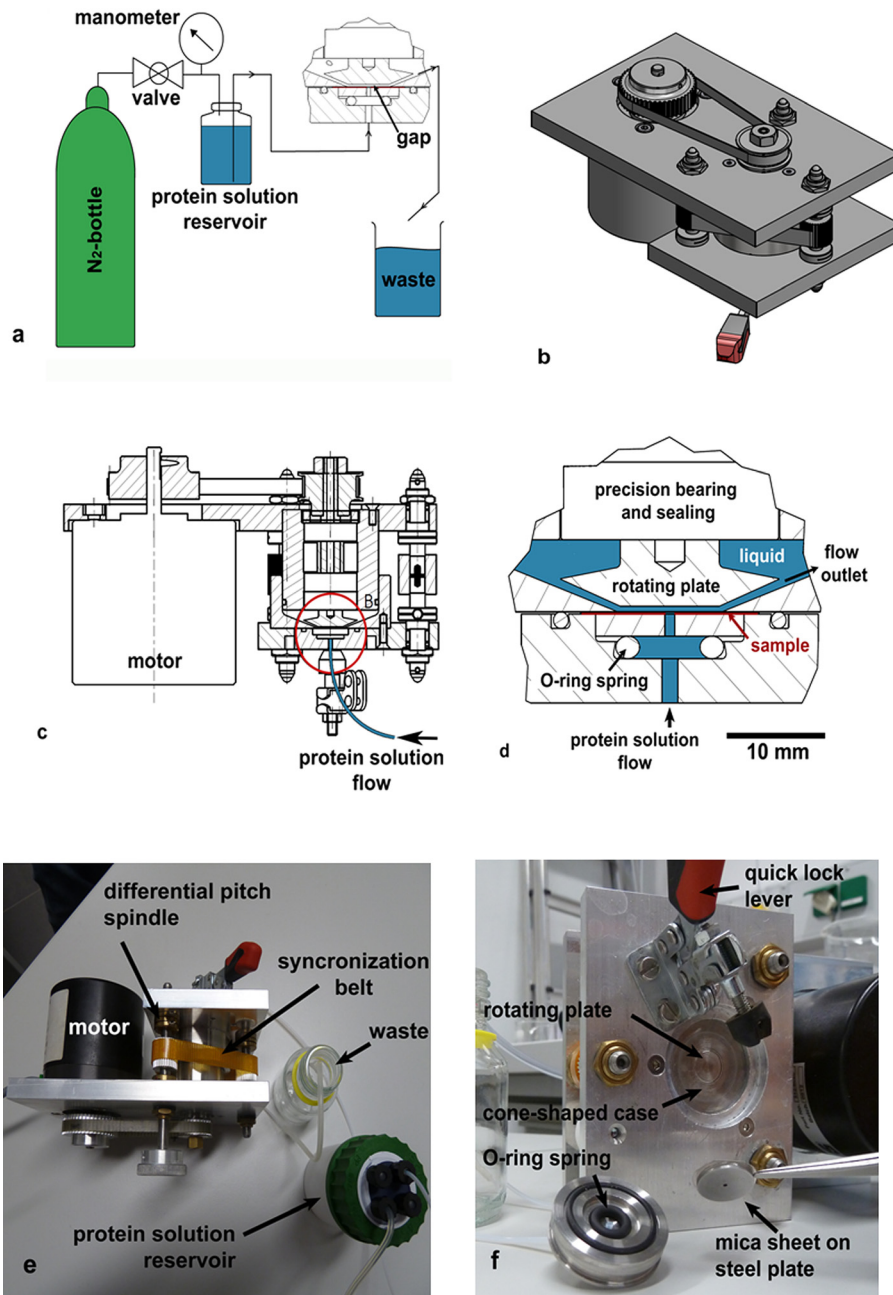


FIG. 2. (a) Experimental setup (schematic). (b) View of the device, showing the gap-width adjusting system. The 3 differential pitch spindles are driven by a precision synchronous belt to permit a parallel movement of the sample relative to the rotating plate. (c) Cross-section: the red circle denotes the details (d) of the geometry of the plate-to-plate rheometer unit. The sample surface (freshly cleaved mica sheet) is colored in red, and the volume filled with VWF solution is marked in blue. The gap width is not to scale. (e) Photograph of the experimental setup. (f) The rotating plate which is planar and vertically adjustable relative to the cone-shaped steel case (gap width adjustment) is shown in detail. The mica sheet, mounted on a steel plate, is pressed to this steel case by an O-ring spring and a steel cap using the quick lock lever.

### A. The shear stress device

The centerpiece of the device (Fig. 2) is a plane rotating plate arranged parallel to the sample-carrying plate [Fig. 2(d)]. The cone shape at the margins should minimize the onset of turbulences. TBS buffer solution containing the protein is fed to the system through a hole in the middle of the sample plate, which consists of a mica plate glued to a polished, plane steel

TABLE I. Parameters used for samples shown in Figs. 2(a)–2(e). The error range for the tangential shear rate is given by the tolerance of the gap width ( $\pm 1 \mu\text{m}$ ), and the error of the radial shear rate is the gap width tolerance plus the time and volume errors of flow measurement.

Sample	a	b	c	d	e
Rotational speed of rotor (RPM)	2100	2341	2578	2817	3054
Liquid flow (ml/min)	5.9	6.6	7.3	8.0	8.6
Shear rate tangential ( $\text{s}^{-1}$ )	21.991	24.511	27.003	29.495	31.986
Shear rate error ( $\text{s}^{-1}$ )	709	791	871	951	1.032

sample holder with epoxy resin. After drilling the central hole, mica sheets were cleaved using adhesive tape, resulting in atomically flat surfaces with occasional steps of some nanometer height (checked by AFM). The precision of the gap in terms of distance and planarity is crucial for obtaining accurate shear rates. Therefore, the rotor is mounted with a spindle bearing arrangement [Figs. 2(b) and 2(c)], and all parts are fabricated from the same steel (X2CrNiMo17-12-2) to prevent differences in thermal dilatation. Furthermore, the geometry [Fig. 2(d)] was optimized to reduce the distance between the fix bearing and the rotor surface with respect to possible thermal disequilibrium caused by friction. Cleaved mica sheets vary in thickness, and therefore, an O-ring was used as a spring to press the sample towards the tapered case with a force of  $\sim 50 \text{ N}$ . The cap, which holds the sample and the spring O-ring and is connected to the feed tubing, is mounted by a toggle lever for quick removal of the sample. The rotation of a DC-motor is transmitted to the rotor by a timing belt drive (gear ratio, 1:1.66) shown in Figs. 2(b) and 2(c).

In order to permit adjusting of the gap size, the steel case is composed of two telescopically fitting parts: the inner one contains the bearing- and sealing-units and the outer one is the inverted cone shaped one, which determines the sample position [Fig. 2(d)]. These two parts are moved parallel to each other by 3 differential pitch spindles synchronized by a toothed belt with a zero-play engagement. Each spindle has two different threads, 0.2 mm and 0.25 mm, resulting in a translation of  $50 \mu\text{m}$  per full turn [Figs. 2(c) and 2(d)].

## B. The setup

The whole setup is depicted in Fig. 2(a). The buffer solution containing VWF is pumped into the device by a gas overpressure in the reservoir. The setup consists of a nitrogen bottle (containing nitrogen quality, 5.0), a ball valve, and a manometer with a scale splitting of 0.1 atmospheres which is connected by 3 mm diameter PE tubes to the pressure resistant reservoir (100 ml PTFE (polytetrafluoroethylene) bottle; max 5 atm). A  $\sim 20 \text{ cm}$  long PTFE tube with an inner diameter of 1 mm connects the reservoir to the plate-to-plate rotor device and serves to supply the gap steadily with the liquid buffer. The outlet consists of another identical PTFE tube.

## C. Determination of the gap size $\tilde{H}$

The gap size was measured off-line using a digital gauge with a precision of  $3 \mu\text{m}$  (Digital, Mitutoyo, Kawasaki, Japan), mounted on a swinging arm capable of pivoting with a plane precision of  $\pm 1 \mu\text{m}$  in a range of  $\sim 2 \text{ cm}$  [tested with a precision parallel block of hardened steel (Norelem, Markgröningen, Germany)]. The immersion of the rotor at the level of the barrel body plane was thereby measured on 4 different positions with intermediate manual rotation. Dry rotation showed that the spindle bearing arrangement and the sealing produced heat, causing a thermal elongation of the rotor of  $\sim 5 \mu\text{m}$  after 1 min of rotation at full speed. In contrast, 10 min of rotation at full speed (5400 RPM) in TBS-buffer solution at room temperature without liquid exchange leads to a tolerable thermal drift of a gap size smaller than  $2 \mu\text{m}$  (this value was certainly drastically lower at the virtually isothermal operating conditions given by the liquid feed). Although these errors would potentially sum up to several  $\mu\text{m}$ , the repeated measurement of the actual gap size at different positions resulted in a planarity of the rotor of less than

$\pm 1 \mu\text{m}$ , and likewise, parallelism between the rotor and the conical steel body (and therefore the rotor and sample) was also  $\pm 1 \mu\text{m}$ , measured at the margins of the rotor (measurement at the margins overestimates the error but keeps the operating region of the rotor untouched). Thus, some potential errors averaged out or were initially overestimated. We used a gap size error of  $\pm 1 \mu\text{m}$  to calculate the error of shear rates.

#### D. Rotating speed $\tilde{\Omega}$

The rotating speed could be adjusted between  $\sim 80$  RPM and 5400 RPM. The used motor (BLDC 58, McLennan servo supplies, Surrey, UK) is equipped with a 36 pulses per round sensor system. Rotating speed was displayed on a pulse counter and could be adjusted with a precision of less than 2 RPM.

#### E. Volume flux $\tilde{Q}$

Radial flow was controlled by the gas pressure measured before the liquid reservoir, which was approximately 0.2 atmospheres. Given the diameter of tubing (3 mm for gas and 1 mm for liquid tubes), the pressure loss between the manometer and the active region of the shear device is negligible when compared to the pressure drop of the flow through the gap. The volume flux was adjusted before the injection of the protein solution and kept constant during the measurement by collecting liquid at the outlet, using a pipette and a stopwatch and averaging over a sufficient time span to achieve errors smaller than  $\pm 1\%$ . The radial contribution to the shear rate is negligible, while the rotation dominates as explained in the “Theoretical part—fluid dynamics in the gap.”

#### F. Quantification of stretching

When VWF is adsorbed on the surface under shear conditions, various phenomena can be observed, including orientation, disentangling of the chains, and elongation. As a parameter to describe all these effects, the quotient of the maximum one-dimensional length and contour length is used, which in the following referred to as the “stretching parameter.” Figure 3 shows exemplarily the determination of the stretching parameter of one individual oligomeric VWF molecule. The stretching parameter essentially describes the linearity of such a chain like molecule, although it also contains indirect information concerning the elongation insofar as linearity is a precondition for stretching, and therefore, an increase in the contour length was observed only in cases with stretching parameters near to 1. Although elongation could be interesting for biological considerations concerning the functionality of VWF, linearity was identified as a more reproducible parameter for the semiquantitative analysis of wall shear rates (for a critical discussion, see Sec. IV).

#### G. AFM-imaging

All AFM images were recorded in the tapping mode (TM) with a NanoScope V (Bruker, Santa Barbara, CA, USA) using etched single crystal silicon probes (NCH from Nanoworld, Neuchatel, Switzerland) with a spring constant of 42 N/m. Images were taken with set points corresponding to a damping of approximately 90% of the free amplitude. Images were recorded at a distance of 3 mm from the rotation center. The image size was  $10 \mu\text{m} \times 10 \mu\text{m}$ , and each image showed a minimum of 120 molecules. For the determination of an average local stretching parameter, all molecules that were totally inside a  $4 \mu\text{m} \times 4 \mu\text{m}$  square (centered on the image) were taken into account. Three independent samples for each shear rate were analyzed.

#### H. Source of recombinant VWF (rVWF)

rVWF is a recombinant human protein expressed in CHO cells and purified to homogeneity. In contrast to VWF fractionated from the human plasma which is always partially proteolyzed, rVWF is an intact VWF molecule and contains the full spectrum of multimers. rVWF

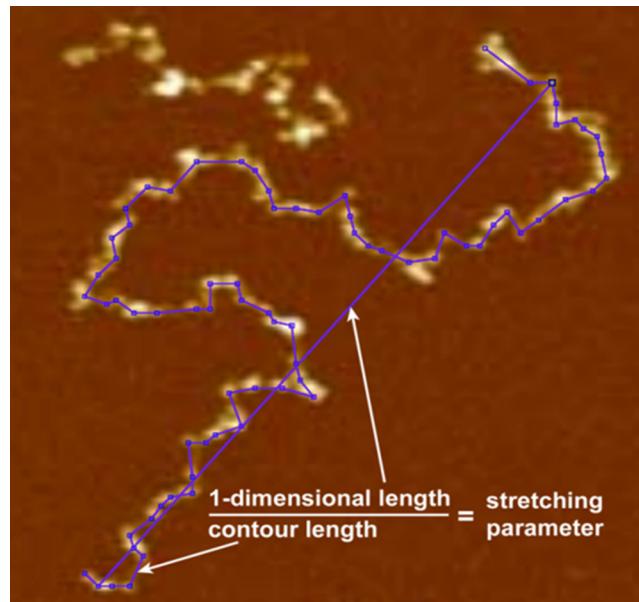


FIG. 3. The AFM image shows exemplarily the determination of the contour length and maximal 1-dimensional length of a sensor molecule. The quotient of the lengths of the straight line and the contour line is the stretching parameter. This is indicative for the linearity and therefore a measure for the stretching of VWF.

was recently licensed under the brand name Vonvendi<sup>®</sup> as a drug product for the treatment of different forms of von Willebrand's disease.<sup>22,23</sup> All AFM studies were conducted with rVWF lot HN02R00 and were carried out under identical conditions as described by Bonazza *et al.*<sup>24</sup>

### III. THEORETICAL PART—FLUID DYNAMICS IN THE GAP

For targeting the scope of this study, it is crucial to maintain well-defined and fully understood flow conditions in the active region of the gap lumen where shear-force-indicating stretching of sensor molecules takes place. The following classical fluid dynamical considerations make clear that, within a certain range of parameters, the situation in the gap can be nicely approximated with satisfactory accuracy as a state of fully developed flow (ideal Couette flow in the circumferential direction).<sup>25,26</sup> Therefore, the mean shear rate used for the comparison with the measurements can be calculated as the local disc speed divided by the gap width. At the parameters which have been chosen for the experiments, no turbulence, flow inversion, or significant heating is expected.

#### A. Reference and dimensionless quantities

The fluid feeding the gap is a highly diluted aqueous buffer solution of sensor molecules. The flow can be handled as incompressible and isoviscous, justified by the almost constant temperature. In the following, dimensional quantities are indicated by tildes. The region of fully developed flow is governed by six input parameters: nominal gap height  $\tilde{H}$ , constant rotational speed  $\tilde{\Omega}$  of the top plate [Figs. 2(b) and 2(d)], pressure-controlled volume flux  $\tilde{Q}$ , ambient temperature  $\tilde{T}_a$  (20°, standard conditions), kinematic viscosity of the solution  $\tilde{\nu}$ , and specific heat capacity of the fluid  $\tilde{c}$  (4.182 kJ kg<sup>-1</sup> K<sup>-1</sup> water at standard conditions), with the latter two being taken as uniform. The characteristic values of  $\tilde{\nu}$ , as well as the linear thermal expansion coefficient of the steel,  $\tilde{\alpha}$ , and the diameter of the hose,  $d$ , are shown in Table II. It should be mentioned that the atomically flat mica surface of the stationary (top) disc is perfectly smooth and the polished one of the rotating (bottom) disc which has grooves of several  $\mu\text{m}$  in width and depth can be viewed sufficiently (i.e., hydraulically) smooth. Moreover, as a consequence of the low flow velocity in the tubing (which also makes any swirl motion negligible), the feed

TABLE II. Constant flow and experimental parameters.

Thermal expansion coefficient steel $\alpha$ ( $10^{-6} \text{ K}^{-1}$ )	Diameter of tubing $d$ (mm)	Gap width $H$ ( $\mu\text{m}$ )	Temperature $T_a$ ( $^{\circ}\text{C}$ )	Prandtl number $Pr$	Radius of sampling $R$ (mm)
11.5	1	30	20	6.99	3

flow is treated as axisymmetric as long as the potential onset of turbulence is delayed far enough downstream from the observed surface area.

Both points are confirmed below: Having chosen an appropriate reference radius  $\tilde{R}$ , the characteristic value  $\tilde{U}$  of the radial flow speed near  $\tilde{r} = \tilde{R}$  and the mean flow speed  $\tilde{U}_h$  in the hose are determined by the imposed volume flux

$$\tilde{Q} := 2\pi\tilde{R}\tilde{H}\tilde{U} = \pi\tilde{d}^2\tilde{U}_h/4. \quad (1)$$

Our starting point for order-of-magnitude estimates is the values of  $\tilde{U}_h$  given in Table I.

By dimensional analysis, the seven relevant dimensional flow parameters  $\tilde{Q}, \tilde{\Omega}, \tilde{R}, \tilde{H}, \tilde{T}_a, \tilde{\nu}$ , and  $\tilde{c}$  are converted into the equivalent four non-dimensional groups: aspect ratio  $\epsilon$ , Reynolds number  $Re_\epsilon$  (as reduced by  $\epsilon^2$ ) Rossby number  $Ro$ , Eckert number  $Ec$ ,

$$\epsilon := \tilde{H}/\tilde{R}, \quad Re_\epsilon := (\epsilon^2 \tilde{U}\tilde{R})/\tilde{\nu}, \quad Ro := \tilde{U}/(\tilde{\Omega}\tilde{R}), \quad Ec := (\tilde{\Omega}\tilde{R})^2/(\tilde{c}\tilde{T}_a). \quad (2)$$

We anticipate at this stage that the Brinkman number  $Br := Ec Pr$  with the Prandtl number  $Pr$  of the fluid given in Table II is so large that internal heating by dissipation can be taken as sufficiently weak. Also, the vertical thermal expansions of the discs are found to only insignificantly alter the nominal gap geometry (see Sec. II). Therefore, thermal effects are confidently taken as negligible. Let  $\tilde{r}$  and  $\tilde{z}$ ,  $\tilde{u}$ ,  $\tilde{v}$ ,  $\tilde{w}$ ,  $\tilde{p}$  (in the specific order) denote the coordinates in radial and vertical directions (their origin coincides with the center of the bottom sample disc),  $\tilde{u}$ ,  $\tilde{v}$ , and  $\tilde{w}$  the components of the fluid velocity in radial, circumferential, and  $z$ -directions, and  $\tilde{p}$  the fluid pressure. We introduce their non-dimensional counterparts as follows:

$$r := \tilde{r}/\tilde{R}, \quad z := \tilde{z}/\tilde{H}, \quad [u, w] := [\tilde{u}, \tilde{w}]/\tilde{U}, \quad v := \tilde{v}/(\tilde{\Omega}\tilde{R}), \quad p := \tilde{p}/(\tilde{\rho}\tilde{U}^2). \quad (3)$$

## B. Problem formulation and order-of-magnitude estimates

Most important, we fix the reference radius  $\tilde{R}$  by setting

$$Re_\epsilon = Ro^2, \quad \text{and applying (1) and (2) yields} \quad (4a)$$

$$\tilde{R} = \sqrt{\tilde{\nu}\tilde{Q}/(2\pi\tilde{H}^3\tilde{Q}^2)}. \quad (4b)$$

This reduces the number of dimensionless groups: Considering  $\tilde{R}$  as a function of  $\tilde{Q}$  and  $\tilde{\Omega}$  yields the potential range of its reference values. The radius  $\tilde{R}$  used in the experiments is 3 mm. It is found that at  $\tilde{R}$  close to 3 mm up to 4.5 mm, the basic assumptions for a fully developed flow in a thin gap

$$\epsilon \ll 1, \quad (5a)$$

$$Re_\epsilon \ll 1, \quad (5b)$$

i.e., negligibly small pressure variations across the gap and vanishingly small inertial effects (Stokes or creeping flow), are perfectly met. Hence, the specific definition (4b) suitably fixes

the section of measurements and so provides the basis for the specific design of the apparatus. Within this range of suitable radii of 3–4.5 mm, the particular operating radius of 3 mm was chosen for practical reasons such as the scanning range of our sample scanning AFM.

This scenario applies indeed if, at the same time, laminar–turbulent transition is safely avoided for  $\tilde{r} < \tilde{R}$ . We note that in a fully developed slender shear layer, the Reynolds number controlling this process is formed with the typical layer thickness, which is here given by  $\text{Re}_H := (\tilde{U}\tilde{H})/\tilde{\nu} = \text{Re}_\epsilon/\epsilon$ , and has to be kept distinctly below a critical threshold, typically of order  $10^3$ . In this sense, transition is suppressed in the feed hose if the corresponding Reynolds number  $\text{Re}_d := \tilde{U}_h\tilde{d}/\tilde{\nu}$  stays markedly below its well-known critical value of about 2250. From (1),

$$\text{Re}_d = 4\tilde{Q}/(\pi\tilde{d}\tilde{\nu}) < 2250, \quad \text{Re}_H = \text{Re}_d\tilde{d}/(8\tilde{R}) \ll \text{Re}_d, \quad (6)$$

which justifies the above issue.

Although the scaling law confirms a sufficient suppression of instabilities before turbulence, it should be mentioned here that a potential time-dependence of the laminar flow has been also considered.  $Ro \ll 1$  can be interpreted as the ratio of two intrinsic time scales  $1/\tilde{\Omega}$  and  $\tilde{R}/\tilde{U}$ , and therefore, the flow in our rheometric device can safely be considered to be in a steady state after a startup phase which, according to the values in Table II, would result in 18 ms. As the typical time for each experiment was in the order of minutes, the requirements for a fully developed stationary flow are met.

### C. Governing equations

Inspection of the Navier-Stokes equations shows that the limits indicated by (5) reduce to those describing an axisymmetric radial Poiseuille flow. Due to the choice (4b) of  $\tilde{R}$ , this is subjected to a pronounced centrifugal force as it is one-sidedly coupled with a Couette flow in the azimuthal direction. It is practically of great value that varying  $\tilde{Q}$  and  $\tilde{\Omega}^2$  proportionally means mechanical similarity of the flow for a given kinematic configuration. Specifically, substitution of the leading order approximations  $[u, v, w] \sim [U, V, \in W](r, z)$  and  $p \sim \text{Re}_\epsilon P(r)$  yields the (parameter-free) simplified momentum equations

$$U_{zz} = P' - V^2/r, \quad (7a)$$

$$V_{zz} = 0. \quad (7b)$$

These are supplemented with the boundary conditions

$$U(r, 0) = U(r, 1) = 0, \quad V(r, 0) = 0, \quad V(r, 1) = r \quad (8)$$

and the requirement of mass conservation in the radial direction according to (1),

$$\int_0^1 rU(r, z)dz = 1, \quad (9)$$

which determines  $P(r)$ . The  $w$ -component of the flow velocity follows from the solution of (7)–(9) by integration of the continuity equation

$$(rU)_r + rW_z = 0. \quad (10)$$

### D. Wall shear rates and radial flow

From (7) and (8), we have

$$U = -P'(r)z(1-z)/2 + rz(1-z^3)/12, \quad (11a)$$

$$V = rz. \quad (11b)$$

The asymmetry of  $U$  in  $z$  with respect to  $z = 1/2$  becomes explicit when the flow is considered in a frame of reference rotating with  $\tilde{\Omega}/2$ : there the skew-symmetric contribution  $rz(1-z)(2z-1)/12$  to  $U$  originates in the  $r$ -component of the Coriolis acceleration  $-r(z-1/2)$  and then enters the right-hand side of (7a). By (9), we obtain  $1 \sim -[p'(r) - 3r/10]r/12$ , whence

$$P(r) - P(1) = 3(r^2 - 1)/20 - 12\ln(r). \quad (12)$$

Therein, and consequently in (11a) and the following, two contributions relevant for small and large values of  $r$  are recognized, with the latter reflecting the impact of the centrifugal force (which increases with  $r$ ) in (7a).

Although the concept of this stretching device is to achieve a Couette flow, for practical reasons, a certain feed flow was necessary, resulting in a small radial flow component. It was crucial to keep the flow in a suitable range. The lower limit of radial flow is given by the indispensable cooling function of the liquid and the short desired residence time of sensor molecules in the gap, whereas the upper limit is marked by flow reversal and a substantial aberration from the Couette flow.

The possibility of backflow can be estimated by considering the signs of the non-dimensional wall shear rates in the  $r$ -direction  $\tau_o := U_z(r, 0)$  (sample or bottom plate) and  $\tau_1 := U_z(r, 1)$  (rotating top disc). They follow from (10) and (11a) as

$$\tau_o = -P^{(r)/2} + r/12 = 6/r - r/15, \quad \tau_1 = P^{(r)/2} - r/4 = -6/r - r/10. \quad (13)$$

Hence, the flow is strictly forward upstream of flow reversal at the stationary (lower) wall, as typical of creeping slender-gap flows and occurring for

$$\tilde{r} \gtrsim \tilde{r}_c := \sqrt{90\tilde{R}}. \quad (14)$$

As a crucial finding, the sensing operation can be taken as reliable only for the values of  $\tilde{r}$  considerably smaller than the critical radius,  $\tilde{r}_c$ . This was considered in the experimental setup by collecting images at  $\tilde{r} = 3$  mm, which is 5 times smaller than the radius of beginning asymmetry (Fig. 4). Moreover, since  $r/Ro$  is the azimuthal component of the wall shear rate, according to (2), the resulting ratios of its components in the  $r$ - and in the azimuthal direction at the sample surface given by  $Ro\tau_o/r$  are in the order of  $Re_\epsilon^{1/2}$  and thus sufficiently small owing to (4a) and (5b). We introduce the local total (scalar) shear rate

$$\tau_t := \sqrt{U_z(r, z)^2 + r/Ro^2}.$$

#### IV. RESULTS AND DISCUSSION

Figure 5(a) shows VWF chains adsorbed at a shear rate of  $22\,000\text{ s}^{-1}$ . They were just slightly affected from shear forces showing a stretching parameter of 0.55, which is very close to that of sensor molecules adsorbed under static conditions (shear rate,  $0\text{ s}^{-1}$ ; stretching parameter, 0.5). By increasing the shear rate stepwise to  $29\,500\text{ s}^{-1}$  [Figs. 5(b)–5(d)], more and more molecules were stretched, resulting in stretching parameters up to 0.73. A further stressing of the sensor molecules at  $32\,000\text{ s}^{-1}$  led to nearly uncovered mica surfaces, probably due to a rupture of molecules, representing the upper limit of shear rates detectable with this method. It should be mentioned that sensor molecules, once they are disentangled, can undergo a real elongation, meaning that they increase their contour length. Although this elongation seems very interesting in terms of their biomechanical properties, in the context of shear rate sensing, we focus on the linearity and the degree of disentangling of chains, which are described by the stretching parameter. The dependence of the stretching parameter from the shear-rate is

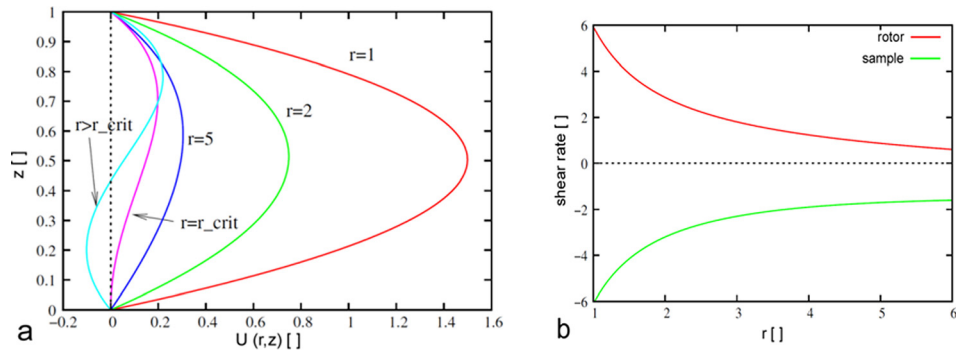


FIG. 4. Symmetry of flow. (a) The dimensionless (normalized) flow profiles for different radii between  $r=1$  ( $r = \tilde{r}/\tilde{R} = 3$  mm, red, used for the experiments) and  $r=5$ ,  $r=r_{crit}$  and a case of flow reversal  $r > r_{crit}$ , reveal the theoretical upper limit of possible radii for data collection (far beyond the actual instrument size). Notable asymmetry and flow reversal (at  $r > r_c$ ) would solely occur at radii above 15 mm. (b) Dimensionless shear rate at the boundaries of the rotor and sample, plotted as a function of radius  $r$ . The slight asymmetry originates from the influence of weak radial flow.

depicted in Fig. 5(f). Above a threshold of about  $22\,000\text{ s}^{-1}$ , the response to the shear rate is linear. It is worth noting that our concept of stretching parameter leads to a value of 0.5 (not zero) at stasis. However, at lower shear rates, a minor radial flow component may play a role.

The theoretical fluid dynamical considerations result in a nearly azimuthal flow direction (small Rossby numbers; small tilting angle,  $\theta$ ) and prove the applicability of the Couette flow

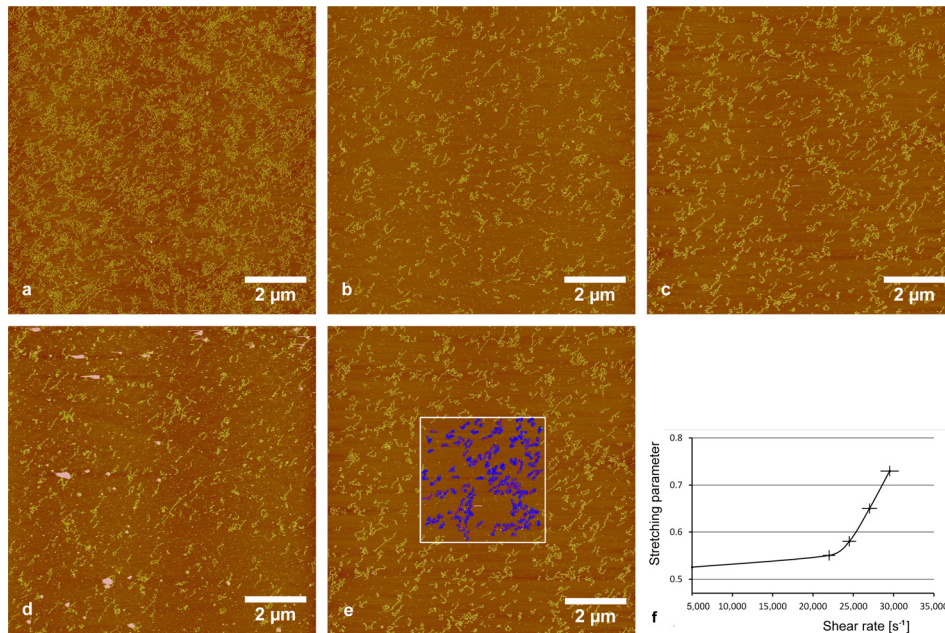


FIG. 5. VWF stretched at increasing shear rates. Characteristic AFM-images from one of the 3 independent experiments taken at a radius of 3 mm are shown. Molecules in (a) ( $22\,000\text{ s}^{-1}$ ) are just slightly affected by the sheared liquid and in (b) ( $24\,500\text{ s}^{-1}$ ) and (c) ( $27\,000\text{ s}^{-1}$ ) are unraveled and oriented in the flux direction. An increase to  $29\,500\text{ s}^{-1}$  shown in (d) caused linearization and elongation. (e) In order to demonstrate the  $4\text{ }\mu\text{m}$  localization of the shear rate measurement,  $4\text{ }\mu\text{m} \times 4\text{ }\mu\text{m}$  spots (white box with blue objects) were used to determine an average stretching parameter as shown here exemplarily. Contour lengths and maximal one-dimensional extensions of molecules were determined using DataLab (see also Sec. II, Fig. 3). All images show a certain background of small dots which are VWF fragments. In (f), the shear rate dependence of the stretching parameter (ratio between the maximum dimension and the contour length) is plotted. For each data point, at least 90 molecules were evaluated, which are derived from 3 independent experiments, giving the vertical error range. Horizontal errors are determined by the tolerance of the gap width. The data below  $5\,000\text{ s}^{-1}$  are not shown in order to avoid over interpretation as the inevitable background radial flow becomes detectable in this regime. (a)–(e) are also available in the [supplementary material](#) for enhanced visibility. Height scale: 5 nm from dark to bright.

approximation, which was used for calculating shear rates (Table I). However, sensor molecules shown in Fig. 5 have much higher  $\theta$ , indicating that they are not totally aligned to the flow trajectories. This can be explained by the short residence time of molecules in the active gap region and the small aspect ratio  $\tilde{H}/\tilde{R}$  of the  $\mu\text{m}$ -scaled gap ( $\tilde{H}$  is just 10 times the length of a sensor molecule), both allowing just a partial reorientation of chains which were exposed to radial acceleration forces in the center/feed region some milliseconds before. Moreover, the orientation of images relative to the azimuthal axis was just roughly adjusted with a precision of  $\pm 15^\circ$ , and therefore, the shear rates should be interpreted as scalars, and tentatively, raw and qualitative, directional information could be extracted. From a nanomechanical point of view, the question may arise, where deformation of sensor molecules takes place, at the surface or in free flowing liquid and at which z-Position? Regarding the first option, it should be mentioned that adhesion of sensor molecules to the mica surface is too weak for proper AFM scanning in liquid, even by the use of the tapping mode with the less invasive parameters (displacement of molecules). This problem has been affronted in numerous studies and is usually circumvented by chemical surface modifications<sup>27,28</sup> or imaging in air;<sup>24</sup> hence, the lack of strong attractive forces between untreated mica and protein molecules is well known. Therefore, our model considers stretching of passively transported sensor molecules by the velocity gradient in the carrying liquid followed by a subsequent deposition on the surface. It is worth noting that an infinitely small particle/molecule, once it comes into contact with the surface, would be trapped due to the boundary condition and therefore virtually adhered to the surface for a diffusion controlled time. In contrast to that, sensor molecules used in this study circulate in liquid as loosely coiled chains with an average sphere-diameter of  $\sim 90\text{ nm}$  as shown by dynamic light scattering.<sup>17</sup> The question at which z-distance from the surface the deformation occurs cannot be answered experimentally in this context; however, the variation of the shear rate in the z-direction is negligible as it is solely caused by the very small radial component of flow. Figure 6 shows the distribution of the shear rate (as a scalar) in the gap with a strongly overscaled (by factor of 10) radial component. Due to this almost linear velocity profile (nearly perfect Couette flow), the z-origin of deposited, stretched molecules is uncritical. It should be mentioned that the radial flow component is still observable for our specific choice of a sensing radius of 3 mm, and thus, in future, an increased radius of up to 4.5 mm seems desirable (as flow reversal or turbulences are still not encountered here) and the choice of radius was influenced by experimental aspects. Although flow reversal would only occur at an operating radius of above 15 mm and is therefore practically excluded, a radius of much more than 4.5 mm (6 mm is geometrically possible but too close to the lateral cone in the present device), which would certainly push the operation range to higher shear rates, seems challenging from an engineering point of view.

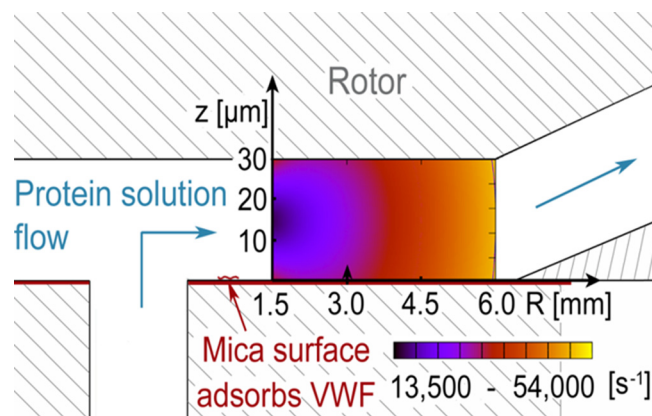


FIG. 6. Calculated distribution of shear rates in the gap shown exemplarily for the sample shown in Fig. 5(c). The radial component is exaggerated for visibility by setting the Rossby number to 0.1. Despite this overdrawn influence of radial motion, the variation of the shear rate in the z-direction at the relevant radius of 3 mm (used for taking images, marked by an arrow) is small. At this radius, the wall shear rate is  $27\,000\text{ s}^{-1}$ .

The image sections used for the determination of the stretching parameter had a size of  $4 \times 4 \mu\text{m}$  and still showed a minimum of  $\sim 30$  molecules, which was necessary for a statistical evaluation. On the one hand, the reliability of shear rate measurements depends on the number of evaluated molecules, and on the other hand, an exaggerated aerial density of molecules would create interpretation problems due to frequently overlapping chains, and thus, a certain minimal size of analyzed images is indispensable. Our results show that the image-size/localization-precision of  $4 \mu\text{m}$  is sufficient for a reproducibility corresponding to a stretching parameter variation of  $\pm 0.01$ .

## V. OUTLOOK

This proof of principle study for the shear rate measurement with sensor molecules in microfluidic devices can now be applied to more complicated geometries with less known flow conditions, always using the described, or an equally simple geometry, as a calibration reference for the stretching-parameter/shear-rate dependence. In the actual version, this method is limited to a certain range of shear rates, suitable for the used sensor molecules. The use of other types of either biological or synthetic macromolecules, as well as a more adhesive coating of the surface, could be a possible way to adapt this concept to any desired shear rate range. Furthermore, improving the theoretical description of the flow by the diffusive transport of the molecules and a more sophisticated modelling of the (non-Newtonian) rheology that accounts for the kinematic degrees of freedom of the macromolecules (Cosserat fluid) seem expedient in follow-up studies.

## SUPPLEMENTARY MATERIAL

See [supplementary material](#) for larger AFM images of stretched sensor molecules.

- <sup>1</sup>G. Onsrud, L. Persen, and L. Sætran, *Exp. Fluids* **5**, 11 (1986).
- <sup>2</sup>H. H. Winter, *Adv. Heat Transfer* **13**, 205 (1977).
- <sup>3</sup>C. Lelièvre, P. Legentilhomme, C. Gaucher, J. Legrand, C. Faille, and T. Bénézéch, *Chem. Eng. Sci.* **57**, 1287 (2002).
- <sup>4</sup>C. Gillham, P. Fryer, A. Hasting, and D. Wilson, *J. Food Eng.* **46**, 199 (2000).
- <sup>5</sup>A. J. Reininger, H. F. Heijnen, H. Schumann, H. M. Specht, W. Schramm, and Z. M. Ruggeri, *Blood* **107**, 3537 (2006).
- <sup>6</sup>C. E. Sing and A. Alexander-Katz, *Biophys. J.* **98**, L35 (2010).
- <sup>7</sup>N. Rajaratnam, *Water Energy Int.* **23**, 137 (1966).
- <sup>8</sup>Z. Wang, *Exp. Fluids* **14**, 153 (1993).
- <sup>9</sup>F. Gijssen, A. Goijaerts, F. Van de Vosse, and J. Janssen, *J. Rheol.* **41**, 995 (1997).
- <sup>10</sup>P. Ireland and T. Jones, *Meas. Sci. Technol.* **11**, 969 (2000).
- <sup>11</sup>K. Shirai, paper presented at the 20th International Congress on Instrumentation in Aerospace Simulation Facilities, Göttingen, Germany, 25–29 August 2003.
- <sup>12</sup>B. B. B. Jensen, A. Friis, T. Bénézéch, P. Legentilhomme, and C. Lelièvre, *Food Bioprod. Process.* **83**, 53 (2005).
- <sup>13</sup>S. W. Hell and J. Wichmann, *Opt. Lett.* **19**, 780 (1994).
- <sup>14</sup>R. Waser, *Nanoelectronics and Information Technology* (Wiley, 2012).
- <sup>15</sup>U. Ulmanella and C.-M. Ho, *Phys. Fluids* **20**, 101512 (2008).
- <sup>16</sup>M. Harrison, W. Batten, L. Myers, and A. Bahaj, *IET Renewable Power Gener.* **4**, 613 (2010).
- <sup>17</sup>E. Di Stasio, F. Romitelli, S. Lancillotti, A. Arcovito, B. Giardina, and R. De Cristofaro, *Biophys. Chem.* **144**, 101 (2009).
- <sup>18</sup>K. Bonazza, H. Rottensteiner, G. Schrenk, C. Fiedler, F. Scheiflinger, G. Allmaier, P. L. Turecek, and G. Friedbacher, *Anal. Bioanal. Chem.* **407**, 6051 (2015).
- <sup>19</sup>S. Schneider, S. Nuschele, A. Wixforth, C. Gorzelanny, A. Alexander-Katz, R. Netz, and M. Schneider, *Proc. Nat. Acad. Sci. U. S. A.* **104**, 7899 (2007).
- <sup>20</sup>T. A. Springer, *Blood* **124**, 1412 (2014).
- <sup>21</sup>K. Bonazza, H. Rottensteiner, G. Schrenk, J. Frank, G. Allmaier, P. L. Turecek, F. Scheiflinger, and G. Friedbacher, *Anal. Chem.* **87**, 10299 (2015).
- <sup>22</sup>P. L. Turecek, G. Schrenk, H. Rottensteiner, K. Varadi, E. Bevers, P. Lenting, N. Ilk, U. B. Sleytr, H. J. Ehrlich, and H. P. Schwarz, *Semin. Thromb. Hemostasis* **36**, 510 (2010).
- <sup>23</sup>P. M. Mannucci, C. Kempton, C. Millar, E. Romond, A. Shapiro, I. Birschmann, M. V. Ragni, J. C. Gill, T. T. Yee, R. Klamroth, W. Y. Wong, M. Chapman, W. Engl, P. L. Turecek, T. M. Suiter, B. M. Ewenstein, and members of the rVWF Ad Hoc Study Group, *Blood* **122**, 648 (2013).
- <sup>24</sup>K. Bonazza, H. Rottensteiner, B. K. Seyfried, G. Schrenk, G. Allmaier, P. L. Turecek, and G. Friedbacher, *Anal. Bioanal. Chem.* **406**, 1411 (2014).
- <sup>25</sup>M. Raghavachari, H.-M. Tsai, K. Kottke-Marchant, and R. E. Marchant, *Colloids Surf. B: Biointerfaces* **19**, 315 (2000).
- <sup>26</sup>J. Adamcik, D. V. Klinov, G. Witz, S. K. Sekatskii, and G. Dietler, *FEBS Lett.* **580**, 5671 (2006).
- <sup>27</sup>H. P. Greenspan, *The Theory of Rotating Fluids*, Cambridge Monographs on Mechanics and Mathematics (Cambridge University Press, 1968).
- <sup>28</sup>R. W. Johnson, *The Handbook of Fluid Dynamics* (CRC Press, 1998).